Proceedings of ASME Turbo Expo 2011
GT2011
June 6-10, 2011, Vancouver, British Columbia, Canada

GT2011-45578

ANISOTROPIC EDDY VISCOSITY IN THE SECONDARY FLOW OF A LOW-SPEED LINEAR TURBINE CASCADE

G. D. MacIsaac[*] and S. A. Sjolander[†]
Department of Mechanical and Aerospace Engineering
Carleton University
Ottawa, Ontario, Canada
gdmacisa@connect.carleton.ca
ssjoland@mae.carleton.ca

ABSTRACT

The final losses within a turbulent flow are realized when eddies completely dissipate to internal energy through viscous interactions. The accurate prediction of the turbulence dissipation, and therefore the losses, requires turbulence models which represent, as accurately as possible, the true flow physics. Eddy viscosity turbulence models, commonly used for design level computations, are based on the Boussinesq approximation and inherently assume the eddy viscosity field is isotropic.

The current paper compares the computational predictions of the flow downstream of a low-speed linear turbine cascade to the experimentally measured results. Steady-state computational simulations were performed using ANSYS CFX v12.0 and employed the shear stress transport (SST) turbulence model with the γ-Re_θ transition model. The experimental data includes measurements of the mean and turbulent flow quantities. Steady pressure measurements were collected using a seven-hole pressure probe and the turbulent flow quantities were measured using a rotatable *x*-type hotwire probe. Data is presented for two axial locations: 120% and 140% of the axial chord (C_x) downstream of the leading edge.

The computed loss distribution and total bladerow losses are compared to the experimental measurements. Differences are noted and a discussion of the flow structures provides insights into the origin of the differences. Contours of the shear eddy viscosity are presented for each axial plane. The secondary flow appears highly anisotropic, demonstrating a fundamental difference between the computed and measured results. This raises questions as to the validity of using two-equation turbulence models, which are based on the Boussinesq approximation, for secondary flow predictions.

*Ph.D. Candidate
†Chancellor's Professor and Pratt & Whitney Canada Research Fellow

INTRODUCTION

The secondary flows of a turbine bladerow are complex and highly three-dimensional, such that the associated losses represent a significant portion of the total bladerow losses. The secondary losses can contribute approximately 1/3 of the total row losses [1] and in low aspect ratio blades this value can increase to as much as 1/2 of the total row losses [2]. For this reason, a reduction of the secondary losses contributes significantly to total loss reduction. An understanding of the fundamental loss production mechanisms is an important first step in reducing the secondary losses.

Past research regarding the details of the secondary flow structures include the works of Sjolander [3], Langston et al. [4], Sieverding [5], Hodson and Dominy [6], Sharma and Butler [7] and Benner [8]. The mechanisms governing secondary loss production have been investigated by Moore and Adhye [9], Gregory-Smith et al. [10] and Harrison [11]. Clearly, turbine secondary flows have been well studied; however, the sources of endwall losses are still not fully understood [12]. More specifically, a complete connection between the mean and turbulent flow field, specific to secondary flows, has yet to be established [13-19]. The final losses within a turbulent flow are realized when turbulent eddies completely dissipate to internal energy through viscous interactions [13]. Therefore, the appropriate modeling of turbulence is necessary to accurately predict the production of total pressure losses in this complex flow field.

In design level computational investigations the turbulent quantities are typically computed using an isotropic eddy viscosity model, which assumes the Reynolds stresses are proportional to the mean velocity gradients. In swirling flows, like the secondary flow through the turbine bladerow, the validity of this assumption is questionable. Although more elaborate computational schemes exist, two-equation eddy viscosity based models are typically considered a satisfactory trade-off between computational accuracy and cost.

The application of endwall contouring to turbine bladerows is one example where computational simulations are used to reduce secondary losses by optimizing the three-dimensional geometry. Computational investigations, employing mixing-length turbulence models to endwall contouring applications by Harvey et al. [20], Hartland et al. [21] and Yan et al. [22], have reported unreliable predictions of the total pressure losses, which suggests inaccuracy in the simulated dissipation of mean kinetic energy to turbulent kinetic energy. Alternative parameters such as the secondary kinetic energy (SKE) and cross-passage static pressure gradient are commonly used as design metrics to assess the benefits from proposed modifications. However, there are reported instances where this is unsuccessful. Ingram et al. [23], despite having used the reduction of the SKE as a design metric for an endwall contouring application, found an increase in the experimentally measured losses. MacIsaac et al. [17] discusses the merit of using the SKE as a design correlation parameter by assessing the contribution of SKE to the downstream mixing losses. In many cases, the SKE does not contribute significantly to the total mixing losses [17]. It is therefore evident that further improvements in our methods of assessing design improvements are desirable.

The production of turbulence is fundamentally the first step to the development of total pressure losses [13]. Studies by Moore et al. [14], Gregory-Smith et al. [13], Gregory-Smith and Cleak [2], Perdichizzi et al. [15], Gustafson et al. [16] and MacIsaac et al. [17] have investigated the turbulent nature of the turbine flow field. Gregory-Smith and Cleak [2] examined the rates at which turbulence, and thus ultimately total pressure losses, were produced from the mean kinetic energy. The Reynolds normal stresses appeared to a make a significant contribution to the loss generating process in the secondary flow region. Similar conclusions are drawn by Moore et al. [14] regarding the normal stresses; however, the $\overline{v'w'}$ shear stresses were also shown to make significant contributions to the dissipation of secondary kinetic energy. MacIsaac et al. [17] presented experimental measurements of turbulence intensity and the rates of turbulence production. It was found that the highest rates of turbulence production, between the counter and passage vortex, were caused by moderate levels of the $\overline{v'w'}$ Reynolds shear stress and high levels of the corresponding gradients. The Reynolds normal stresses did not appear significant to the loss generating process. From these studies, there does not appear to be a unified understanding of the role of the normal and shear Reynolds stress to total pressure loss production in cascade flows, suggesting that the influence of turbulence is not yet fully understood.

In attempts to validate the isotropic eddy viscosity assumptions of commonly used two-equation turbulence models, different conclusions based on the measured eddy viscosity fields have also been reported. Gregory-Smith and Cleak [2] show that the eddy viscosity is reasonably isotropic downstream of the cascade in the secondary flow region. However, Perdichizzi et al.'s [15] results, at higher outlet velocities (Mach 0.3), show that the eddy viscosity of the secondary flow region is highly anisotropic downstream of the cascade. Only at axial locations farther downstream, after significant mixing has taken place, were isotropic conditions obtained.

The current study can be regarded as an extension of the work by MacIsaac et al. [17] and will examine the anisotropy of the eddy viscosity field. The ensuing discussion and analysis is based on the same experimental data, but also includes the results of a complimentary CFD study. The purpose of the computational study was to assess the short-comings of typical design level computational tools.

Measurements of the mean and turbulent flow field have been collected using a seven-hole pressure probe and an *x*-type hotwire probe at two axial locations. Steady-state RANS simulations of the experimental conditions were performed using the SST turbulence model with the ANSYS CFX γ-Re$_\theta$-v-12.0 transition model. The discussion will first examine the differences between experimentally measured flow field and the CFD results. Secondly, the downstream measured eddy viscosities will be examined in relation to the computed eddy viscosity. Comments are made regarding the validity of the Boussinesq eddy viscosity assumption within secondary flows.

EXPERIMENTAL APPARATUS AND PROCEDURES

Test Section and Cascade

The experimental investigation was conducted in the low-speed linear cascade test facility at Carleton University [24-27]. The facility consists of an open circuit wind tunnel that is interfaced with a modular test section. The modular test section is shown in Figure 1 with a linear cascade mounted to a turntable. A turbulence generating grid is located upstream to obtain an inlet free stream turbulence intensity of approximately 3.3% with an integral length scale that is about 25% of the axial chord for the current cascade.

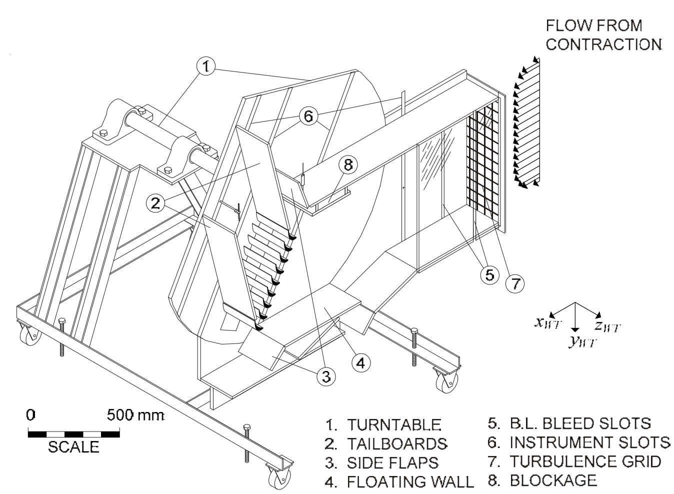

Figure 1. Test section schematic

Two linear actuators automate the movement of the measurement probe in the pitchwise and spanwise directions with a minimum step size of 0.00635 mm. A typical downstream measurement grid consists of 90 pitchwise points collected at 62 spanwise locations, totalling 5580 data points. The minimum spanwise location (nearest to the endwall) is set to 1% span.

This facility has previously been used for a number of studies that have examined both the profile and secondary flow of several turbine cascades [24-27]. Therefore, the experiment and procedures are considered well developed.

The geometric details and design parameters of the test cascade are provided in Table 1. The cascade consists of six blades and measurements are collected for the centre passage. The overall cascade turning at mid-span is 104.7° with inlet and outlet design flow angles of 31.5° and -73.2° respectively. The acceleration through this passage is relatively high as the convergence ratio, *CR*, is about 2.95. The airfoils have a Zweifel coefficient of about 0.97.

Table 1. Cascade geometry

Chord, *C* [mm]	102.1
Axial chord, C_x [mm]	73.3
Pitch, s [mm]	107.2
Span, h [mm]	203.2
Inlet design flow angle, β_1 [°]	31.5
Outlet design flow angle, β_2 [°]	-73.2
Pressure side tangent stagger angle, γ [°]	46.2
Number of blades	6

The schematic drawing in Figure 2 shows the two Cartesian coordinate systems used in this work. The origin of the cascade coordinate system is located at the blade leading edge with the *x*-axis aligned with the axial direction, the *y*-axis with the pitchwise direction and *z*-axis with the spanwise direction relative to the bladerow. In the mean flow coordinate system the x'-axis is aligned with the primary mean flow direction (streamwise) and y' and z'-axis with the secondary velocity directions. The primary flow direction is evaluated using the area-averaged axial and pitchwise velocities at the outlet measurement plane.

$$\overline{\overline{\beta_2}} = \tan^{-1}\left(\overline{\overline{V_2}}\Big/\overline{\overline{U_2}}\right) \quad (1)$$

Instrumentation and Data Acquisition

Pressure Measurements. A maximum of eight *Data Instruments* differential pressure transducers (ASG DRAL505DN), each with a full-scale operating range of ±1250Pa, were used for the pneumatic pressure measurements. The estimated uncertainty for the recorded pressure is ±0.25% of the full scale range. The transducer voltage signal is recorded using a *United Electronic Industries, Inc.* data acquisition card (Power DAQ PD2-MFS-8-800/14). At each data point, 10,000 samples were collected at a rate of 1kHz.

Hot-wire Anemometry. The *x*-type hot-wire probe was connected to two channels, one per wire, of an *A.A Lab Systems*

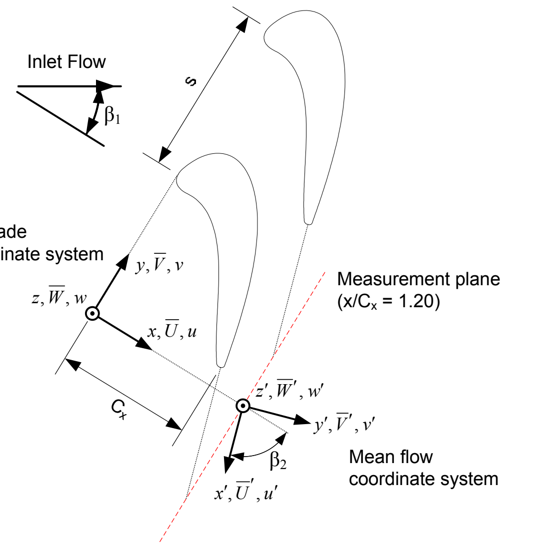

Figure 2. Cascade nomenclature showing the cascade and mean flow coordinate systems

(model AN-1003) constant temperature anemometry system. The overheat ratio (OHR) was set to approximately 1.5. Experimental measurements were made by collecting 131,072 samples at a rate of 28kHz.

Measurement Probes. The inlet endwall boundary layer was traversed using a Pitot probe. The probe diameter relative to the boundary layer thickness is about 3.5%. The estimated uncertainty of the measured total pressure is approximately ±0.3% of the inlet mid-span dynamic pressure. A seven-hole pressure probe is used to make downstream measurements of the total pressure, static pressure and the three components of velocity. The probe tip has an outer diameter of 1.83 mm which equates to a spatial resolution of d/s=0.017 and d/h=0.009 relative to the blade pitch and span respectively. The seven-hole probe was calibrated through the angle range of $-45° < \alpha, \beta < +45°$ in 2° increments for five separate velocities (20, 25, 30, 35 and 42 m/s) to account for Reynolds number affects on the dynamic pressure coefficient [28]. The calibration and data reduction procedures for the seven-hole probe have been adapted from Gerner et al. [29]. The estimated uncertainty of the measured flow angles is ±0.5° and the uncertainties of the measured total and dynamic pressure is ±0.4% of the inlet reference pressure.

The rotatable *x*-type hotwire probe is used to measure the three local velocity components and the six Reynolds stresses. The *x*-type probe consists of four prongs mounted to a probe stem with a nominal diameter of 2.37mm or d/s=0.02 and d/h=0.01. To make measurements in a three dimensional flow field, the calibration of the *x*-type hot-wire requires a velocity and directional sensitivity or angular calibration. The velocity calibration was preformed over the range of $5 < V_{jet} < 45$ m/s. The angular calibration is used to generate the directional sensitivity functions for each wire, $g_i(\alpha, \beta)$, where *i* is the wire number and $-45° < \alpha, \beta < +45°$ in 2° increments. A method detailed by Döbbeling [30], originally derived for quadruple-wire probes, was adapted for the x-type probe used in this experiment. If the angular calibration is performed twice, once with the probe in the 0° roll position and once with the probe rolled through 90°, the two sensors of the x-type probe will mimic the four sensors of a quadruple-wire probe. Since the wire signals cannot be recorded simultaneously for the two orientations of the probe, this method cannot provide instantaneous information regarding the flow field. Therefore, to extract the turbulence data a separate procedure by Buresti [31] was applied. This procedure is based on the general response equation of the hot-wire sensor and involves solving an over-determined non-linear system of equations. To improve the conditioning of the coefficient matrix, additional data were collected at a third roll orientation of 45°. The estimated uncertainties (determined through repeatability studies) of the measured velocities and flow angles are ±1 m/s and ±1.0° respectively.

Operating Conditions. The wind tunnel operating point was set to an inlet Reynolds number of approximately 50,000 based on the blade axial chord. For this cascade the outlet Reynolds number was therefore approximately 150,000.

COMPUTATIONAL PROCEDURES

Domain Geometry

The flow through the cascade was modelled from $1.5C_x$ upstream to $3.0C_x$ downstream of the blade leading edge for one flow passage and one half-span, taking advantage of the cascade pitchwise periodicity and spanwise symmetry. The axial position of the inlet and outlet boundaries can influence the solution results, particularly if the boundaries are chosen too closely to regions of interest. Simulations were performed for domains of varying axial length; the current domain geometry was shown to have negligible effects on the flow variables at the measurement planes of interest ($1.20C_x$ and $1.40C_x$ relative to the blade leading edge).

Mesh

A structured HOH type grid of hexahedral elements was created using ANSYS ICEM CFD v12.0. A hexahedral grid was selected to reduce the overall node count as well as control the wall normal expansion ratio, the grid orthogonality and the maximum/minimum element aspect ratio. The mesh was designed to conform to the requirements of the ANSYS CFX-v-12.0 solver [32] including those of the CFX transition model [33, 34]. Table 2 summarizes the mesh requirements and the corresponding values of the current mesh.

A grid independence study was first conducted on a two-dimensional mid-span plane, simulating the profile flow region. The total pressure, static pressure and dynamic pressure at axial planes of $1.20C_x$ and $1.40C_x$ from simulations using various grids were used to examine the solution results. After achieving grid-independent results the profile grid was extruded over one half-span. The first node spacing on the blade and endwall surfaces was set such that the maximum y+ was approximately 1 as required by the transition model [33, 34]. All wall normal expansion ratios were set to values below 1.1, a requirement again imposed by the transition model [34]. The completed mesh has approximately $7.7\text{x}10^6$ nodes and $7.5\text{x}10^6$ hexahedral elements. The extracted downstream planes have 250 pitchwise points and 115 spanwise points.

Table 2. Summary of the computational mesh parameters

Parameter	*CFX solver requirements* [36]	*Current Mesh*
Edge Length Ratio:	*< 100*	*100**
Min Face Angle:	*> 10°*	*38°*
Element Volume Ratio:	*< 5*	*2.8*

Fluid Model and Boundary Conditions

The steady-state RANS equations were solved with air modelled as an incompressible ideal gas at a constant temperature of 25°C. The domain walls were considered adiabatic and thus the energy equation was not solved. The two-equation SST turbulence model was chosen for this study as it is a widely used model and is based on Boussinesq eddy viscosity assumption. The predicted eddy viscosity distribution is therefore isotropic, and thus this model provides a good example of the effects this assumption has on the prediction of flows in turbomachinery cascades. There are many turbulence models that are based on this assumption, so the selection of SST model is discussed further. The secondary flow development is strongly dependent on prediction of the near wall flow physics. The SST model was designed to provide more accurate prediction of near wall flows in adverse pressure gradients by accounting for the transport of the turbulent shear stresses [33]. To avoid the undesirable sensitivity of the k-ω model to the predictions of the free stream specific turbulence dissipation rate, ω, the SST model switches between the standard k-ω formulation in the near-wall regions to the k-ε model in the outer wake regions and free-shear layers using blending functions [33]. The transition model, γ-Re_θ CFX-v-12.0, was enabled to capture the laminar and turbulent region of the boundary layers on both the blade and endwall surfaces.

The inlet boundary condition was specified from the experimentally measured velocity profile, shown in Figure 3 (a), oriented at the design inlet flow angle of -31.5°. The profile was measured at $-1.20C_x$ at three pitchwise locations, y/s=0.25, 0.5 and 0.75, using a boundary layer pitot probe and endwall static taps. There is minimal pitchwise variation of the inlet boundary layer profile; the lower velocities towards midspan are caused by the inlet turbulence generating grid. The observed variations are consistent with previous work performed by Knezevici et al. [26, 27]. The boundary layer parameters are presented in Table 3.

Spanwise profiles of turbulence kinetic energy (k) and specific turbulence dissipation rate (ω) define the inlet turbulence boundary conditions. In a two-equation k-ω model these two parameters define the length scale, eddy viscosity and turbulence dissipation rate (ε). The turbulence profiles were determined by separately simulating the growth of the

* The edge length ratio exceeds the recommend value in regions very close to the blade and endwall surfaces. This is expected and permissible by the solver provided the simulations are preformed using double precision [32].

boundary layer upstream of the cascade. Iteratively, the boundary layer parameters (thickness, momentum thickness and displacement thickness) and the free-stream value of the turbulence kinetic energy were matched as closely as possible to that of the experiment. It was found that matching the length scale, in addition to the other parameters, was quite difficult. Therefore, the distribution of inlet specific turbulence dissipation rate, ω, was scaled such that the free-stream length scale would match the experimentally determined value. The spanwise turbulence profiles are shown in Figure 3 (b). The ANSYS CFX-v-12.0 solver computes the turbulence intensity and the turbulence length scale to determine the specific turbulence dissipation rate (ω) and the turbulence kinetic energy (k) using equation (2) and (3) respectively [32].

$$Tu_{loc} = \frac{\sqrt{2/3\,k}}{\tilde{U}_{loc}} \tag{2}$$

$$\Lambda/C_x = \frac{k^{1/2}}{C_\mu \omega} \frac{1}{C_x} \tag{3}$$

Table 3. Summary of the inlet boundary layer parameters

Boundary Layer:	Boundary layer thickness	δ/h	0.092
	Displacement thickness (mm)	δ^*	2.13
	Momentum thickness (mm)	θ	1.62
	Boundary layer shape factor	H_{SF}	1.32
	Free stream turbulence intensity	Tu_{loc}	3.3%
	Free stream length scale	Λ/C_x	0.25

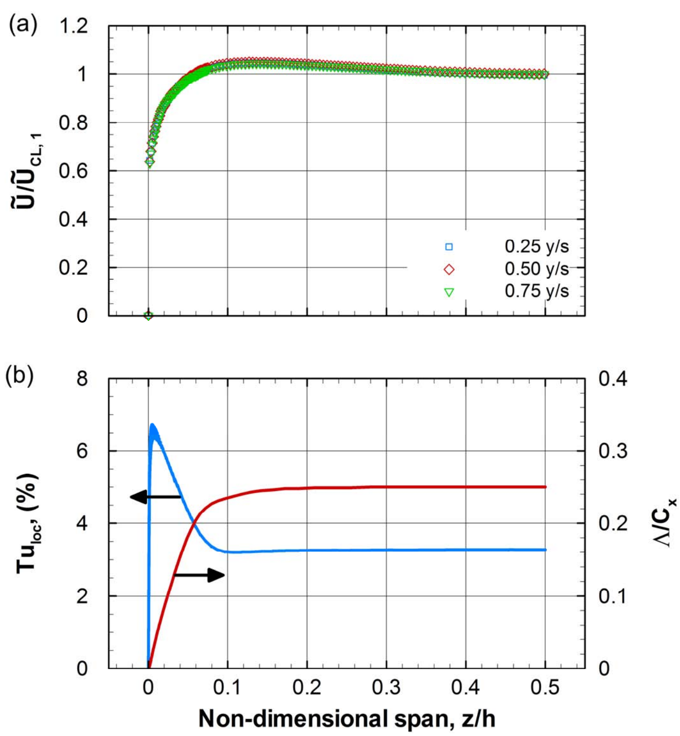

Figure 3. (a) Inlet boundary layer profile measured at −1.20C_x and 0.25, 0.50 and 0.75 y/s (b) inlet turbulence boundary conditions

Solver and Convergence Control

Computational simulations were performed for this study using the ANSYS CFX-v-12.0 solver. The solver implements an element-based finite volume technique in which the mass and momentum equations are satisfied for each mesh volume [32]. The CFX solver is considered a pressure-based, coupled solver that utilizes an Algebraic Multigrid technique [32]. The mass and momentum advection terms are discretized using a second-order differencing scheme. The transitional turbulence terms were discretized using a high resolution (bounded second-order upwind biased) scheme [32].

Solution convergence was judged based on the absolute normalized residuals of the mass, momentum and turbulence equations. When the absolute values of maximum residuals were less than 1.0x10^{-6}, the solution was deemed converged. Typically, this resulted in RMS residuals less than 1.0x10^{-8}.

RESULTS AND DISCUSSION

Blade Loading Distributions

Figure 4 shows the measured and computed loading distributions at mid-span, z/h=0.5, as a fraction of the maximum surface length, S_{max}. The blade surface static pressure coefficient is defined as follows:

$$C_{PS,1} = \frac{P_{0\,CL,1} - P_i}{q_{CL,1}} \tag{4}$$

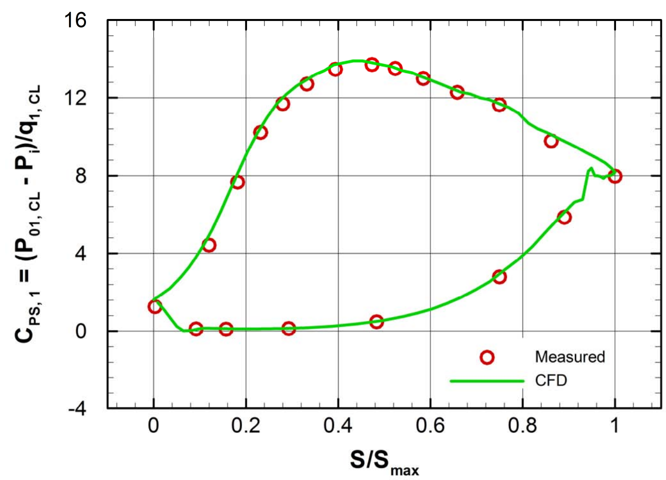

Figure 4. Measured and computed blade surface static pressure distribution at z/h=0.5

The measured and computed loading distributions are similar, indicating that the free stream boundary conditions of the simulations have been well matched to the experiment. The outlet dynamic pressure at S/S_{max}=1.0, is also similar to the experimental value, indicating that the domain outlet boundary location is not affecting the simulation results. The suction surface peak is located at approximately S/S_{max}=0.48 and there appears to be a small separation bubble that extends from S/S_{max}=0.65 to 0.85. The computational loadings support this observation; however, the velocity vectors do not show a region of reversed flow. This apparent bubble is a region of very low shear stress.

Downstream Results

The Experimental and Computational Flow Field. Pressure and turbulence measurements were made over one full pitch and one half-span at the $1.20C_x$ and $1.40C_x$ axial planes using a seven-hole pressure probe and a rotatable x-type hotwire probe respectively. The corresponding CFD results were extracted at the axial planes of interest. Figure 5 shows floods of the total pressure coefficient, defined as,

$$C_{P0} = \frac{P_0 - P_{0\,CL,1}}{q_{CL,1}} \quad (5)$$

and represents the local total pressure loss relative to the upstream ($-1.20C_x$) midspan reference value. Here, the high loss regions are represented by red, lower loss regions by blue and no loss regions by white.

Figure 6 presents floods of the streamwise vorticity coefficient at the same axial locations. The streamwise vorticity coefficient, defined as,

$$C_{\omega s} = C_{\omega x} \cos \overline{\overline{\beta_2}} + C_{\omega y} \sin \overline{\overline{\beta_2}} \quad (6)$$

where,

$$C_{\omega_x} = \frac{\omega_x C_x}{\tilde{U}_{CL,1}},\ C_{\omega_y} = \frac{\omega_y C_x}{\tilde{U}_{CL,1}} \quad (7)$$

represents the local rotation of the fluid relative to the streamwise direction. Thus, the yellow and red regions indicate a negative rotation about the streamwise axis while the green and blue regions represent a positive rotation. The secondary velocity vectors are also shown in Figure 6.

MacIsaac et al. [17] discussed the evolution of this flow downstream of the cascade with reference to the streamwise vorticity and the secondary kinetic energy coefficient. The current paper will focus on the comparison between the measured and computed results.

Figures 5 (a) and (b) show the total pressure coefficients from the $1.20C_x$ axial plane. In the measured results in Figure 5 (a), there is one distinct loss core, labelled A, located at about y/s=0.18 and z/h=0.17. This region of high loss does not coincide with any of the major vortical structures, as seen from Figure 6 (a). The passage vortex, shown in red, is located at y/s=0.22 and z/h=0.07, the counter vortex, shown is green, is at y/s=0.16 and z/h=0.14, and the corner vortex was located too close to the endwall to be adequately resolved. The peak loss is concentrated in the region of high shear between the passage vortex and the counter vortex. MacIsaac et al. [17] indicated that the strong spanwise and cross passage flow, as shown by the secondary velocity vectors in Figure 6 (a), tends to sweep the low momentum fluid from the endwall boundary layer up the suction surface of the blade. Thus, the peak loss core appears to be a combination of low momentum fluid from the inlet endwall and suction surface boundary layers and the additional losses generated through the dissipation of some of the secondary kinetic energy.

The corresponding computed total pressure coefficients are shown in Figure 5 (b). The highest computed losses are located very close to the endwall, at about y/s=0.28 and z/h=0.1. However, this region is too close to the endwall to be measured. Therefore, the following discussion will concentrate on the large region of high losses away from the endwall. The predicted losses in this region are much greater in magnitude and are more highly concentrated than for the measured results. The peak loss, labelled A, is about 22% higher than the measured and is located slightly more towards midspan, at y/s=0.18 and z/h=0.18. Unlike for the measured results, the peak loss is nearly coincident with the location of the counter vortex, at y/s=0.17 and z/h=0.18, suggesting that significant loss production is predicted to occur within the vortex. The computations also show two additional distinct loss cores, labelled B and C. Loss core B is located above the counter vortex and coincides with a region of lower negative streamwise vorticity, as shown in Figure 6 (b). This structure appears as a weak coherent vortex core in the computations but is not observed experimentally. In the experimental flow such a structure may already have been dissipated by viscous action or have become entrained by the counter-vortex. Loss core C is considerably weaker than the other two and is local to the passage vortex, as shown from Figure 6 (b). The measurements also show a total pressure deficit in the passage vortex region, although the magnitude is again lower than in the computations.

In general, it appears that the vortical structures have diffused significantly more in the measurements than the computations at the downstream plane. This diffusion has also reduced the peak losses observed in the measurements. At the same time, a region of high loss production exists in the highly sheared flow between the passage and counter vortices. This is the region of the highest measured losses. High loss production in this inter-vortex region is likely also present in the computations, and may be the origin of the tail of high losses associated with loss core A in Figure 5(b). However, the highly concentrated vortices and the corresponding high losses in the predictions seem to mask this inter-vortex loss production.

The results for $1.40C_x$ plane show considerable diffusion of the vortices and reductions in the peak losses compared with the $1.20C_x$ plane, for both the measured and computed results. For example, the measured streamwise vorticity associated with the passage vortex, is reduced by approximately 40%, while the predictions show a reduction of about 17%. Similarly, the peak streamwise vorticity for the counter vortex is reduced by 38% for the measurements and 28% for the computed results. This confirms that the diffusion of the vortical structures occurs much more quickly in the experiment than in the computations.

Integrated Downstream Results. The integrated flow field quantities were computed for each axial location. Area- and mass-averages are computed at cell centres as follows:

Area-averaged: $$\overline{\overline{\Omega}} = \frac{1}{A}\int_0^{0.5}\int_0^1 \Omega\, dy dz \quad (8)$$

Mass-averaged: $$\Omega'' = \frac{\rho}{\dot{m}}\int_0^{0.5}\int_0^1 \bar{U}\Omega\, dy dz \quad (9)$$

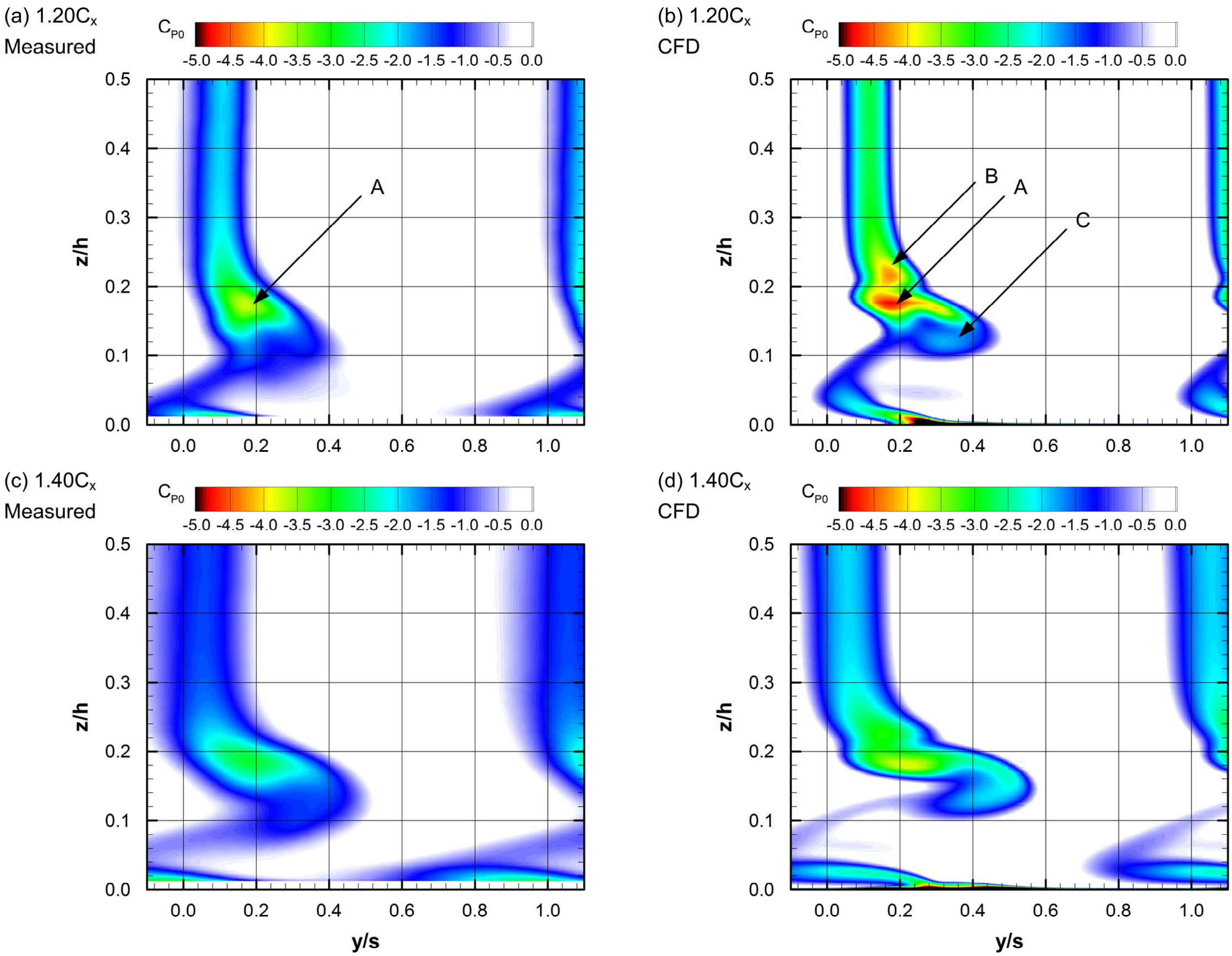

Figure 5. Measured and computed total pressure coefficient (C_{P0}) floods at 1.20C_x and 1.40C_x

The experimental results require an approximation for the total pressure at the endwall, z/h=0. It is assumed that the static pressure gradient normal to the wall is zero and the total pressure at the endwall is then taken as the static pressure measured with the probe at z/h=0.01. The results for fully-mixed out conditions were also calculated using the procedure of Harrison [11]. This computation assumes that the mixing occurs at constant area and neglects the additional loss production due to the shear stress at the endwall.

The integrated results from the two axial planes are summarized in Table 4. Figure 7 shows the relative magnitudes of the flow quantities, normalized by the measured mass-averaged total pressure coefficient from the respective planes. At 1.20C_x and 1.40C_x the measured mass-averaged total pressure loss is 5.7% and 7.5% greater than the computed values respectively. This result appears surprising given that the computed peak losses are much higher than the measured values (for example, 22% higher for the 1.20C_x plane). It seems to be the result of two effects. Firstly, the measured losses are somewhat more widely distributed because of the higher diffusion than for the computed flow. Secondly, the axial velocities, and thus the local mass flow rates, are noticeably lower in the high loss regions for the computed results. The net effect is that the mass-averaged losses are actually slightly higher for the measured results.

The results from the 1.20C_x plane show good agreement between the mixed-out values of total pressure loss for the measurements and computations. The dissipation of the secondary kinetic energy makes a significant contribution to these mixed-out losses. The higher secondary kinetic energy for the computed flow thus partly made up for the lower measured losses to give similar final mixed-out losses. At the 1.40C_x plane the predicted mixed-out losses agree less well with those from the measurements. It is also evident that mixing out of the secondary kinetic energy, though significant, still accounts for only about 60% of the additional loss

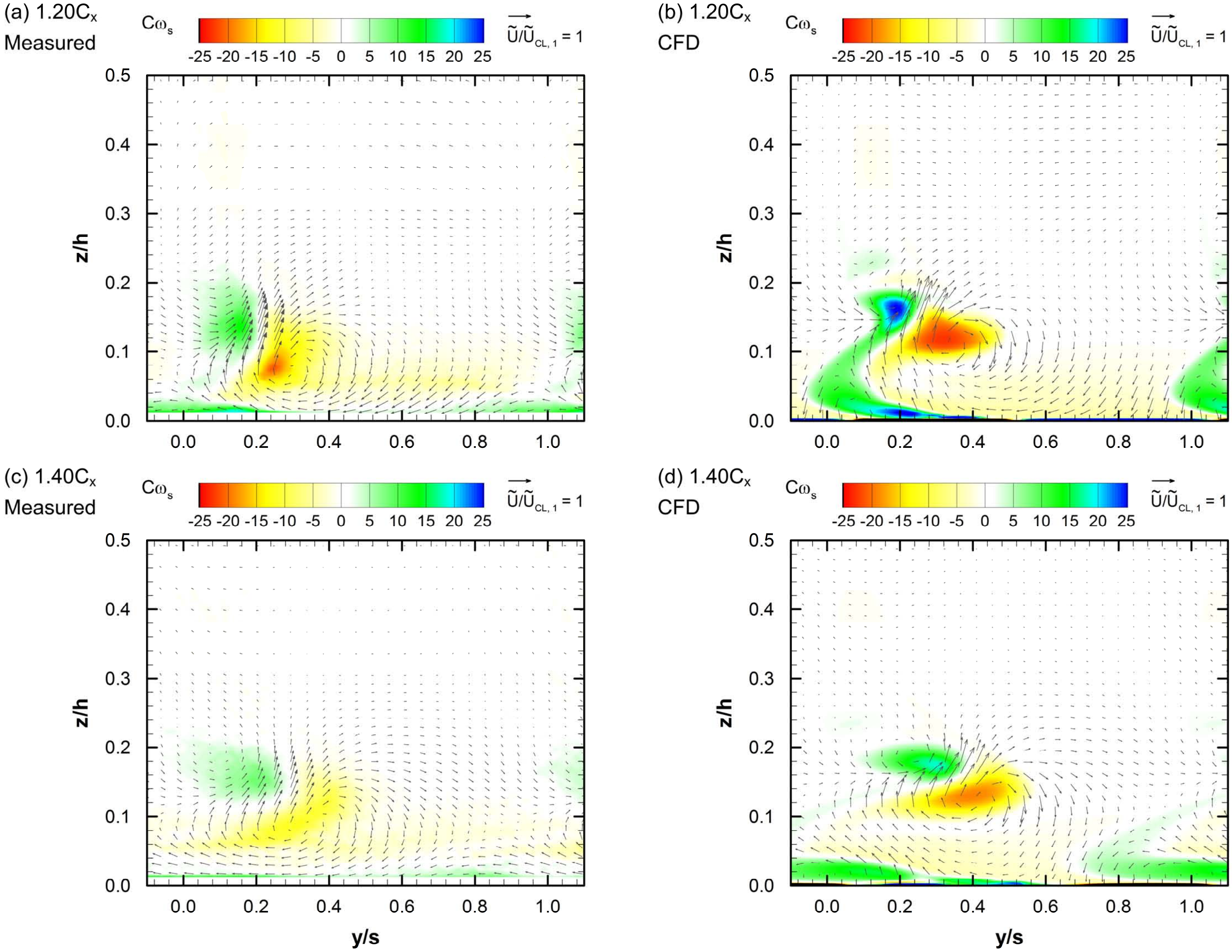

Figure 6. Measured and computed streamwise vorticity coefficient ($C_{\omega s}$) floods and secondary velocity vectors at 1.20C_x and 1.40C_x

Table 4. Summary of the integrated flow quantities

Parameter	*Measured*		*CFD*	
	1.20C_x	*1.40C_x*	*1.20C_x*	*1.40C_x*
C_{P0}''	-0.422	-0.464	-0.398	-0.429
$C_{P0,\,mixed}''$	-0.500	-0.544	-0.481	-0.498
$\overline{\overline{C_{SKE}}}$	0.040	0.034	0.059	0.042
$\overline{\overline{C_{TKE}}}$	0.022	0.022	-0.398	-0.429

*The uncertainty of integrated losses are ±0.0035 with a 95% level of confidence [8].

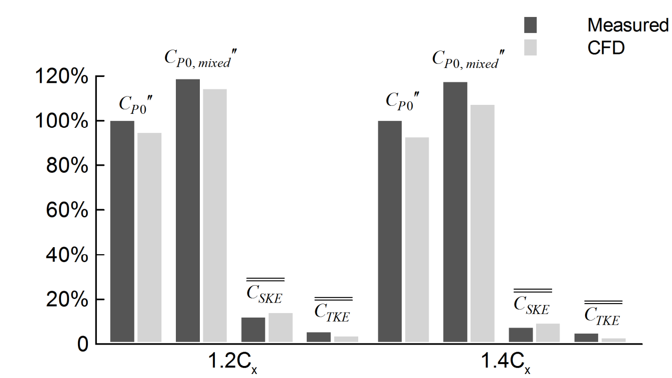

Figure 7. Normalized total pressure loss, mixed out total pressure and secondary kinetic energy coefficients

generated through mixing. Some additional loss would also be expected from the mixing out of the non-uniformities in the primary flow field. There can also be a loss contribution from the non-uniform static pressure in the measurement plane. The observation that mixing out of the secondary kinetic energy only accounts for a portion of the additional losses has implications for the use of the secondary kinetic energy as a metric for evaluating the success of design modifications, such as end wall contouring. It has been common to judge such modifications as a success if they leave a lower level of secondary kinetic energy in the flow than the baseline case, on the basis that the result will be a lower final loss. The present results show that secondary kinetic energy is an imperfect metric: there are additional significant sources of further loss production, over and above dissipation of the secondary kinetic energy.

Table 4 and Figure 7 also includes values of the area-averaged turbulent kinetic energy coefficient, obtained from the hot-wire measurements and defined as,

$$C_{TKE} = \frac{1}{2}\frac{\left(\overline{u^2}+\overline{v^2}+\overline{w^2}\right)}{\tilde{U}^2_{CL,1}} \tag{10}$$

This represents energy extracted from the mean flow and not yet dissipated to internal energy. The measured C_{TKE} shows negligible change between the two measurement planes, indicating that the turbulence is being produced from the mean flow at a similar rate to that at which it is being dissipated by viscous action [17]. This is not the case in the computations. The predicted turbulent kinetic energy is reduced by about 15% from the $1.20C_x$ to the $1.40C_x$ plane. This is evidently one of the reasons that the computations predict the development of the losses with downstream distance somewhat inaccurately.

The turbulence eddy viscosity. As seen, compared with the computations the measured results show higher levels of turbulent kinetic energy, greater rates of kinetic energy dissipation, higher integrated losses, and more diffuse loss distributions. Losses are realized first through the production of turbulence from the mean flow and then ultimately by dissipation of the resulting turbulence [13]. In typical computational simulations, an eddy viscosity-based turbulence model relates the Reynolds stress tensor in the RANS equations to the mean strain stain tensor, $S_{i,j}$, using a scalar value of the eddy viscosity, ν_T, according to

$$-\overline{u_i u_j} = 2\nu_T S_{i,j} - \tfrac{2}{3}k\delta_{i,j} \tag{11}$$

Thus, the eddy viscosity is isotropic. Schmitt [35] discusses the validity of this assumption in general turbulent flows. He concludes that the wide range of turbulence length scales observed in turbulent flows invalidates the computation of stress based on a single mean scale [35]. An eddy viscosity tensor might provide some directional sensitivity, but would still be an oversimplification of the complexity of the turbulence. In general, it is recognized that the assumption of isotropic eddy viscosity is a weakness of the turbulence models commonly used in engineering design. The hot-wire measurements allow the actual degree of anisotropy of the effective eddy viscosity to be investigated in the present flow.

The computed scalar eddy viscosity for the SST turbulence model used in the present computations is given by

$$\nu_T/\nu_L = \frac{a_1 k}{\max(a_1\omega,\ SF_2)}\frac{1}{\nu_L} \tag{12}$$

where a_1 is a constant, F_2 is a blending function that restricts the production limiter to the near-wall boundary layer and S is the magnitude of the strain rate,

$$S_{i,j} = \frac{1}{2}\left(\frac{\partial \overline{U}'_i}{\partial x'_j}+\frac{\partial \overline{U}'_j}{\partial x'_i}\right) \tag{14}$$

The measured effective eddy viscosity (the “eddy viscosity tensor”) is obtained from the data using

$$\nu_{i,j}/\nu_L = \frac{-\overline{u'_i u'_j}}{2S_{i,j}}\frac{1}{\nu_L} \tag{13}$$

The analysis is confined here to the Reynolds shear stresses. Both the computed and measured eddy viscosities are non-dimensionalized by the kinematic viscosity, ν_L. Expressions for the mean axial velocity gradients are calculated using a method similar to that used by Gregory-Smith et al. [10] and Yaras and Sjolander [36] for determining the vorticity components from experimental data.

The predicted eddy viscosities at the $1.20C_x$ plane are shown in Figure 8 as a colour-flood contour plot, overlaid with line contours of the total pressure coefficient. Comparisons with the floods of streamwise vorticity in Figure 6 (b) indicate that the peak values of eddy viscosity occur in the vortical structures. The maximum value is located within the passage vortex, at y/s=0.32 and z/h=0.12, and is approximately 150 times the laminar viscosity. In the turbulence model (see Equation (12)), the high value of eddy viscosity would tend to be associated with elevated turbulence kinetic energy and high Reynolds shear stress. However, MacIsaac et al. [17] showed that in the experiment the highest rates of turbulence production occur in the high shear region between the passage and counter vortices, rather than within the vortices themselves.

The measured values of the effective eddy viscosity components are shown in Figures 9 (a) to (c). Note that the scale of the measured eddy viscosity is twice that used for the computed values in Figure 8. The data reduction procedure for the measured results involves the division of the Reynolds stress by the mean strain rate, $S_{i,j}$. The latter is difficult to determine accurately in regions of low shear strain rate. Consequently, in regions where both the mean strain rate and the corresponding Reynolds stress were small the eddy viscosity was set to zero. As a further check, pitchwise distributions of the terms in Equation (13) were examined for a number of spanwise locations. An example of such distributions is shown in Figure 10 for z/h=0.10. This figure will be discussed further below.

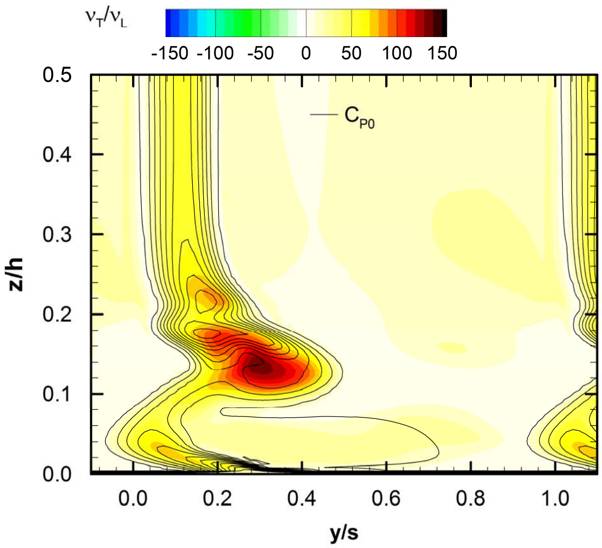

Figure 8. Predicted non-dimensional eddy viscosity at 1.20C_x

The colour-flood contour plot in Figure 9 (a) shows the eddy viscosity that corresponds to the $\overline{u'v'}$ Reynolds shear stress at the 1.20C_x plane. The line contours are again the total pressure coefficient. Moderate levels of the eddy viscosity are found within the wake region, with slightly higher values on the suction-surface side of the wake. The magnitudes are approximately 100 times the laminar viscosity, which are roughly twice the computed values obtained in the wake (see Figure 8). The under-prediction of the eddy viscosity, $\nu_{1,2}$, within the wake region results in lower shear stresses and consequently less mixing with the free stream fluid. As observed in Figure 5, the computed results in the wake region did show higher peak losses and less diffusion compared with the measurements.

Within the secondary flow, at a pitchwise location of approximately y/s=0.2, there exists a thin region of high positive eddy viscosity, $\nu_{1,2}$, with an adjacent region of apparently negative eddy viscosity. A negative eddy viscosity is physically counter-intuitive, at least in a two-dimensional shear flow, since it implies momentum transport against the mean velocity gradient. This is borne out in the wake region where only positive values of the eddy viscosity are obtained.

Figure 10 shows that the negative eddy viscosities are local to regions in which the mean strain rate and Reynolds shear stress are changing sign, at 0.16< y/s < 0.20, such that the mean strain rate and the Reynolds shear stress are briefly both negative. It appears that the eddy viscosity assumption is not adequate in this localized region. Perdichizzi et al. [15] also showed negative values of the measured eddy viscosity, for the $\overline{u'w'}$ component, and suggested that the eddy viscosity assumption may not be valid in the secondary flow region.

Figure 9 (b) shows the eddy viscosity corresponding to the $\overline{u'w'}$ Reynolds shear stress. The maximum eddy viscosity is approximately 400 times the laminar viscosity and is located in

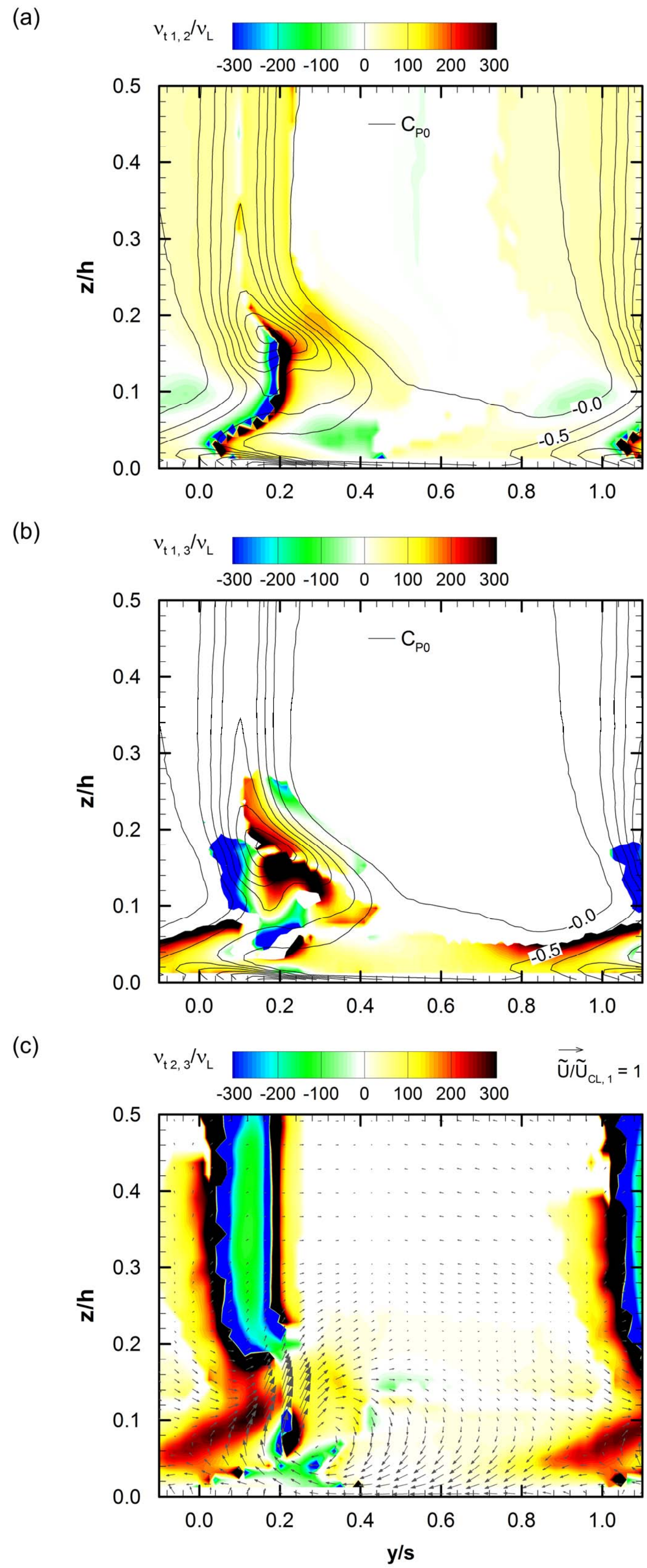

Figure 9. Floods of the measured non-dimensional shear eddy viscosity at 1.20C_x

the high shear region between the passage and the counter vortex. This distribution includes even larger magnitudes of negative eddy viscosity. Similar distributions to those in Figure 10, but at z/h=0.14, show that very large negative values of $\overline{u'w'}$ were measured in this region together with very small positive mean strain rates, which yield large negative eddy viscosities. The signs of the mean strain rates are somewhat suspect when the strain rates are small, due to experimental uncertainty. However, it is worth pointing out that where negative eddy viscosities were obtained, in all cases presented here, they were obtained consistently from the measurements at a significant number of adjacent measurement points in both the spanwise and pitchwise directions. The positive eddy viscosities are not suspect since they are the result of large positive Reynolds stresses and significant negative mean strain rates. Again, the results raise questions about the validity of the isotropic eddy viscosity approximation in the secondary flow region.

Figure 9 (c) shows the measured eddy viscosities corresponding to the $\overline{v'w'}$ component of the Reynolds shear stress. Even more significant regions of negative eddy viscosities are observed and they now include the two-dimensional wake region. Furthermore, the negative values are obtained in regions where the local mean strain rates and Reynolds stresses are of significant magnitude. This makes them harder to dismiss. The region of positive eddy viscosity within the secondary flow is located where the passage and counter vortices begin to interact, at y/s=0.04 and z/h=0.10. This is a region of high shear, as noted from the secondary velocity vectors. MacIsaac et al. [17] showed that this is the region with the highest rates of turbulence production and thus significant rates of total pressure loss production. The computed results also show elevated values of the eddy viscosity in the corresponding location, although of lower magnitude than measured.

Together, Figures 9 (a) to (c) show very significant anisotropy in the three components of the eddy viscosities corresponding to the Reynolds shear stresses. The peak measured eddy viscosities are also approximately three times larger than those obtained with the turbulence model. Finally, significant regions of negative eddy viscosity were obtained, which, while counter-intuitive, appear to be difficult to dismiss.

CONCLUSIONS

Experimental measurements of the mean and turbulent flow fields have been obtained downstream of a low-speed linear turbine cascade. The flow field is compared to corresponding CFD results to assess the prediction capabilities of computations that employ eddy viscosity turbulence models. In particular, the validity of the assumption of isotropic eddy viscosity was assessed.

The computational results show high peak losses that are local to vortical structures within the secondary flow. The measured results show significantly lower peak losses. Furthermore, these peak losses did not coincide with either the passage or counter vortices but occurred instead in the high shear regions where these two vortices interact. The computational results showed at least one weak vortical structure that was not observed experimentally. Overall, the measured results showed the higher rates of diffusion for both the wakes and three-dimensional flow features compared with the predictions.

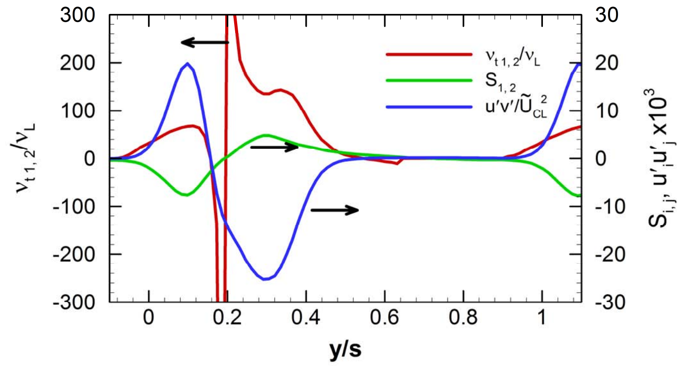

Figure 10. Non-dimensional eddy viscosity, mean strain rate and Reynolds stress at 1.20C_x and z/h=0.10

Secondary kinetic energy is often used to judge the success of a design modification, with lower predicted or measured secondary kinetic energy being taken to indicate lower additional losses yet to be generated through mixing. While the secondary kinetic energy does make a significant contribution to the mixing losses, for the present flow it only accounted for about 60% of the subsequent mixing losses. Thus, secondary kinetic energy appears to be an imperfect metric to use in assessing design modifications.

Detailed comparisons between the measured and predicted eddy viscosities were made at the 1.20C_x plane. The eddy viscosity downstream of the cascade was found to be highly anisotropic, particularly within the secondary flow region. The peak magnitudes of the eddy viscosities associated with the shear stresses were also found to be approximately three times larger than those generated by the turbulence model. Finally, significant regions of negative eddy viscosity were obtained. Although, negative eddy viscosities are counter-intuitive physically, they were obtained at large numbers of adjacent measurement locations and are therefore difficult to dismiss.

ACKNOWLEDGMENTS

The first author gratefully acknowledges the financial support of the National Sciences and Engineering Research Council (NSERC) of Canada through NSERC Postgraduate Scholarships and the Government of Ontario through Ontario Graduate Scholarships (OGS). Financial support from NSERC in the form of a Discovery Grant is also gratefully acknowledged by the second author. Useful technical discussions with Dr. T. Praisner of Pratt & Whitney Aircraft, East Hartford, CT. are acknowledged.

NOMENCLATURE

A	Area, $\int_0^{0.5}\int_0^1 dydz$
C	True chord
CR	Convergence ratio, $\cos\beta_1/\cos\beta_2$
C_x	Axial chord
C_{P0}	Total pressure coefficient, see Eq. (5)
$C_{P0,\ mixed}$	Mixed-out total pressure coefficient
C_{SKE}	Secondary kinetic energy coeff., $\left(\overline{V}'^2+\overline{W}'^2\right)\Big/\tilde{U}_{CL,1}^2$
C_{TKE}	Turbulent kinetic energy coefficient, see Eq. (10)
$C_{\omega s}$	Streamwise vorticity coefficient, see Eq. (6)
C_μ	k-ε turbulence model constant, 0.09
d	Probe tip diameter
H_{SF}	Shape factor
h	Span
k	Turbulence kinetic energy
$\dot{m}$	Mass flow rate, $\rho\int_0^{0.5}\int_0^1 \bar{U}dydz$
P_0	Total pressure
P_S	Static pressure
q	Dynamic pressure
Re	Reynolds number, $\tilde{U}_{CL,1}C_x/\nu_L$
s	Pitch
S	Surface length
$S_{i,j}$	Mean strain rate, see Eq. (14)
Tu	Turbulence intensity, see Eq. (2)
U_i	Velocity vector
$\tilde{U}$	Resultant velocity vector, $\sqrt{\overline{U}^2+\overline{V}^2+\overline{W}^2}$
U, V, W	Cartesian velocity components
u, v, w	Cartesian turbulent fluctuations
x, y, z	Axial, pitchwise and spanwise directions
y+	Non-dimensional distance from the wall, $\Delta y u_\tau/\nu_L$
Zw	Zweifel coefficient, $\frac{2s}{C_x}\cos^2\beta_2\left(\tan\beta_2-\frac{C_{a1}}{C_{a2}}\tan\beta_1\right)$
Λ	Turbulence length scale, see Eq. (3)
α	Yaw or spanwise flow angle
β	Pitch or pitchwise flow angle (from axial)
δ	Boundary layer thickness
δ^*	Displacement thickness
ε	Turbulence dissipation rate
γ	Pressure side tangent stagger angle
ν	Kinematic viscosity
ρ	Density
θ	Momentum thickness
ω	Specific turbulence dissipation rate

Superscripts

$'$	Mean flow coordinate system
$''$	Mass-averaged flow quantity
$\overline{}$	Time-averaged flow quantity
$=$	Area-averaged flow quantity

Subscripts

1, 2	Upstream and downstream
CL	Centre line of blade span, z/h=0.5
i	Wire number
L	Laminar
loc	local
T	Turbulent
WT	Wind tunnel coordinate system

REFERENCES

[1] Denton, J. D., 1993, “The 1993 IGTI Scholar Lecture: Loss Mechanisms in Turbomachines,” ASME J. Turbomach., **115**, pp. 621-656.

[2] Gregory-Smith, D. G. and Cleak, J. G. E., 1992, “Secondary Flow Measurements in a Turbine Cascade with High Inlet Turbulence,” ASME J. Turbomach., **114**, pp. 173-183.

[3] Sjolander, S. A., 1975, “The Endwall Boundary Layer in an Annular Cascade of Turbine Nozzle Guide Vanes,” M.Eng. thesis, Carleton University, Ottawa.

[4] Langston, L. S., Nice, M. L. and Hooper, R. M., 1976, “Three-Dimensional Flow within a Turbine Cascade Passage,” ASME Paper No. 76-GT-50, Mar. 21-25.

[5] Sieverding, C. H., 1985, “Recent Progress in the Understanding of Basic Aspects of Secondary Flows in Turbine Blade Passages,” ASME Journal of Engineering for Gas Turbines and Power, **107**, pp. 248-257.

[6] Hodson, H. P. and Dominy, R. G., 1987, “Three-Dimensional Flow in a Low-Pressure Turbine Cascade at Its Design Condition,” ASME J. Turbomach., **109**, pp. 177-185.

[7] Sharma, O. P. and Butler, T. L., 1987, “Predictions of Endwall Losses and Secondary Flows in Axial Flow Turbine Cascades,” ASME J. Turbomach., **109**, pp. 229-236.

[8] Benner, M. W., 2003, “The Effects of Leading Edge Geometry on Profile and Secondary Losses in Turbine Cascades,” PhD thesis, Carleton University, Ottawa, Canada.

[9] Moore, J. and Adhye, R. Y., 1985, “Secondary Flows and Losses Downstream of a Turbine Cascade,” ASME Journal of Engineering for Gas Turbines and Power, **107**, pp. 961-968.

[10] Gregory-Smith, D. G., Graves, C. P. and Walsh, J. A., 1988, “Growth of Secondary Losses and Vorticity in an Axial Turbine Cascade,” ASME J. Turbomach., **110**, pp. 1-8.

[11] Harrison, S., 1990, “Secondary Loss Generation in a Linear Cascade of High-Turning Turbine Blades,” ASME J. Turbomach., **112**, pp. 618-624.

[12] Praisner, T. J., Allen-Bradley, E., Grover, E. A., Knezevici, D. C. and Sjolander, S. A., 2007, “Application of Non-Axisymmetric Endwall Contouring to Conventional and High-Lift Turbine Airfoils,” ASME Paper No. GT2007-27579, Montreal, Que., Canada, May 14-17.

[13] Gregory-Smith, D. G., Walsh, J. A., Graves, C. P. and Fulton, K. P., 1988, “Turbulence Measurements and Secondary Flows in a Turbine Rotor Cascade,” ASME J. Turbomach., **110**, pp. 479-485.

[14] Moore, J., Shaffer, D. M. and Moore, J. G., 1987, “Reynolds Stresses and Dissipation Mechanisms Downstream of a Turbine Cascade,” ASME J. Turbomach., **109**, pp. 258-267.

[15] Perdichizzi, A., Ubaldi, M. and Zunino, P., 1992, “Reynolds Stress Distribution Downstream of a Turbine Cascade,” Experimental Thermal and Fluid Science, **5**, pp. 338-350.

[16] Gustafson, R., Mahmood, G. and Acharya, S., 2007, “Aerodynamic Measurements in a Linear Turbine Blade Passage

with Three-Dimensional Endwall Contouring," ASME Paper No. GT2007-28073, Montreal, Que., Canada, May 14-17.

[17] MacIsaac, G. D., Sjolander, S. A. and Praisner, T. J., 2010, "Measurements of Losses and Reynolds Stresses in the Secondary Flow Downstream of a Low-Speed Linear Turbine Cascade," ASME Paper No. GT-2010-22727, Glasgow, UK, June 14-18.

[18] Porreca, L., Hollenstein, M., Kalfas, A. I. and Abhari, R. S., 2007, "Turbulence Measurements and Analysis in a Multistage Axial Turbine," Journal of Propulsion and Power, **23**, pp. 227-234.

[19] Vicharelli, A. and Eaton, J. K., 2006, "Turbulence Measurements in a Transonic Two-Passage Turbine Cascade," Experiments in Fluids, **40**, pp. 897-917.

[20] Harvey, N. W., Rose, M. G., Taylor, M. D., Shahpar, S., Hartland, J. and Gregory-Smith, D. G., 2000, "Nonaxisymmetric Turbine End Wall Design: Part I- Three-Dimensional Linear Design System," ASME J. Turbomach., **122**, pp. 278-285.

[21] Hartland, J. C., Gregory-Smith, D. G., Harvey, N. W. and Rose, M. G., 2000, "Nonaxisymmetric Turbine End Wall Design: Part II- Experimental Validation," ASME J. Turbomach., **122**, pp. 286-293.

[22] Yan, J., Gregory-Smith, D. and Walker, P. J., 1999, "Secondary Flow Reduction in a Nozzle Guide Vane by Non-Axisymmetric End-Wall Contouring," ASME Paper No. 99-GT-339, Indianapolis, Indiana, USA, June 7-10.

[23] Ingram, G., Gregory-Smith, D. and Harvey, N., 2005, "Investigation of a Novel Secondary Flow Feature in a Turbine Cascade with End Wall Profiling," ASME J. Turbomach., **127**, pp. 209-214.

[24] Zoric, T., Popovic, I., Sjolander, S. A., Praisner, T. and Grover, E., 2007, "Comparative Investigation of Three Highly Loaded LP Turbine Airfoils: Part I - Measured Profile and Secondary Losses at Design Incidence," ASME Paper No. GT2007-27537, Montreal, Que., Canada, May 14-17.

[25] Zoric, T., Popovic, I., Sjolander, S. A., Praisner, T. and Grover, E., 2007, "Comparative Investigation of Three Highly Loaded LP Turbine Airfoils: Part II - Measured Profile and Secondary Losses at Off-Design Incidence," ASME Paper No. GT2007-27538, Montreal, Que., Canada, May 14-17.

[26] Knezevici, D. C., Sjolander, S. A., Praisner, T. J., Allen-Bradley, E. and Grover, E. A., 2010, "Measurements of Secondary Losses in a Turbine Cascade with the Implementation of Nonaxisymmetric Endwall Contouring," ASME J. Turbomach., **132**, 011013.

[27] Knezevici, D. C., Sjolander, S. A., Praisner, T. J., Allen-Bradley, E. and Graver, E. A., 2009, "Measurements of Secondary Losses in a High-Lift Front-Loaded Turbine Cascade with the Implementation of Non-Axisymmetric Endwall Contouring," ASME Paper No. GT2009-59677, Orlando, FL, USA, June 8-12.

[28] MacIsaac, G. D., Taremi, F., Knezevici, D. C., Scribner, C. A. and Sjolander, S. A., 2009, "Challenges in Using Kiel and Seven-Hole Pressure Probes in Highly Three-Dimensional Flows: Application to Turbomachinery Cascade Measurements," 19^{th} ISABE Conference Paper No. ISABE-2009-1209, Montreal, QC, Sept. 11-17.

[29] Gerner, A. A., Maurer, C. L. and Gallington, R. W., 1984, "Non-Nulling Seven-Hole Probes for High Angle Flow Measurement," Experiments in Fluids, **2**, pp. 95-103.

[30] Döebbeling, K., Lenze, B. and Leuckel, W., 1990, "Computer-Aided Calibration and Measurements with a Quadruple Hotwire Probe," Experiments in Fluids, **8**, pp. 257-262.

[31] Buresti, G. and Di Cocco, N. R., 1987, "Hot-Wire Measurement Procedures and their Appraisal through a Simulation Technique," Journal of Physics E: Scientific Instruments, **20**, pp. 87-99.

[32] ANSYS Inc., 2009, "Ansys CFX-Solver Theory Guide," ANSYS CFX, Release 12.0.

[33] Menter, F. R., Langtry, R. B., Likki, S. R., Suzen, Y. B., Huang, P. G. and Volker, S., 2006, "A Correlation-Based Transition Model Using Local Variables - Part I: Model Formulation," ASME J. Turbomach., **128**, pp. 413-422.

[34] Langtry, R. B., Menter, F. R., Likki, S. R., Suzen, Y. B., Huang, P. G. and Volker, S., 2006, "A Correlation-Based Transition Model Using Local Variables - Part II: Test Cases and Industrial Applications," ASME J. of Turbomach., **128**, pp. 423-434.

[35] Schmitt, F. G., 2007, "About Boussinesq's Turbulent Viscosity Hypothesis: Historical Remarks and a Direct Evaluation of Its Validity," C. R. Mécanique, **335**, pp. 617-627.

[36] Yaras, M. and Sjolander, S. A., 1990, "Development of the Tip-Leakage Flow Downstream of a Planar Cascade of Turbine Blades: Vorticity Field," ASME J. Turbomach., **112**, pp. 609-617.